ARTICLE   **OPEN**

Check for updates

North Atlantic Oscillation impact on the Atlantic Meridional Overturning Circulation shaped by the mean state

Hyo-Jeong Kim[1], Soon-Il An[2,3,4 ✉], Jae-Heung Park[4], Mi-Kyung Sung[5], Daehyun Kim[6], Yeonju Choi[3] and Jin-Soo Kim[1]

Accurate representation of the Atlantic Meridional Overturning Circulation (AMOC) in global climate models is crucial for reliable future climate predictions and projections. In this study, we used 42 coupled atmosphere–ocean global climate models to analyze low-frequency variability of the AMOC driven by the North Atlantic Oscillation (NAO). Our results showed that the influence of the simulated NAO on the AMOC differs significantly between the models. We showed that the large intermodel diversity originates from the diverse oceanic mean state, especially over the subpolar North Atlantic (SPNA), where deep water formation of the AMOC occurs. For some models, the climatological sea ice extent covers a wide area of the SPNA and restrains efficient air–sea interactions, making the AMOC less sensitive to the NAO. In the models without the sea-ice-covered SPNA, the upper-ocean mean stratification critically affects the relationship between the NAO and AMOC by regulating the AMOC sensitivity to surface buoyancy forcing. Our results pinpoint the oceanic mean state as an aspect of climate model simulations that must be improved for an accurate understanding of the AMOC.

INTRODUCTION

The Atlantic Meridional Overturning Circulation (AMOC) is one of the key drivers of global climate variability and change, owing to its significant role in global heat redistribution. Studies have shown that a strengthening of the AMOC leads to warming and cooling in the northern and southern hemispheres, respectively[1–6], with such changes further shaping various aspects of the surface climate, such as the European summer temperatures[7], Atlantic hurricane activity[8,9], mid-latitude jet intensity[10,11], latitude of the Intertropical Convergence Zone[12–15], and African/Asian/Indian monsoons[16–19]. Due to its wide-ranging climatic influence, the AMOC also has significant socioeconomic impacts, affecting harvest and fisheries[20–23]. Therefore, an accurate prediction of future AMOC change is required to minimize climate risk for the sake of socioeconomics.

Generating accurate and reliable future predictions and projections of the AMOC requires a full understanding of its: (i) response to various external forcing (e.g., orbital configurations, meltwater flux from ice sheets, and greenhouse gas concentration) and (ii) internal dynamics. The former has been intensively studied in the context of increasing greenhouse gas concentrations, leading to the current consensus that the mean AMOC intensity will weaken in response to greenhouse gas-induced warming[24–30]. This is because greenhouse warming is likely to enhance the stratification of the ocean in the North Atlantic, through increases in surface heat[31,32] and freshwater[33,34] fluxes (i.e., precipitation–evaporation and runoff). However, the internal dynamics of the AMOC are not yet fully understood[35], despite being considered a crucial factor for decadal-scale climate predictions as a slow-varying component of the climate system[36,37].

Because direct observations of the AMOC are limited, researchers have used climate models as a tool to improve knowledge of the variability of the AMOC; using model-based approaches, various mechanisms explaining the AMOC variability have been proposed. Some studies suggested that oceanic processes such as freshwater supply from the Arctic[38] and the interaction between sea surface temperature (SST) variability and density-driven circulation anomalies[39–42] are key processes underlying its variability. Other studies have stressed the role of the atmosphere by considering AMOC variability as an atmospheric noise-driven linear oscillator[43] or an air–sea coupled mode at the interdecadal timescale[44–46].

The North Atlantic Oscillation (NAO) is a widely known atmospheric factor that contributes to changes seen in the AMOC[36,45,47–55]. Although the NAO has been better recognized for its sub-seasonal variability, which is much shorter compared to the timescale at which ocean circulation varies[56], observations show that it also exhibits annual and longer timescale variabilities[36,57,58]. These variabilities could physically influence the decadal and longer variability of the AMOC. For example, the NAO can modulate the AMOC intensity through changes in surface buoyancy fluxes in the deep water formation regions[59–64]; that is, the Labrador[65–68] and Irminger Seas, Iceland basin[69,70] (we shall refer the above regions as the subpolar North Atlantic [SPNA]), and Nordic Seas[68,71]. In ocean-only models, in which atmospheric NAO forcing is prescribed, the AMOC changes driven by the NAO are consistently simulated where it is often portrayed as positive peaks when the NAO precedes[48,53,55] in lagged correlations between smoothed NAO and AMOC indices. However, ocean–atmosphere coupled global climate models (CGCMs) show a wide range in the magnitude of the correlation and the time lag in which maximum correlation appears, with many models underestimating the correlation compared to ocean-only models[36,55,72]. Such large uncertainty in the NAO–AMOC relationship in CGCMs could be attributed to various factors. For example,

[1]Low-Carbon and Climate Impact Research Centre, School of Energy and Environment, City University of Hong Kong, Tat Chee Ave, Kowloon Tong, Hong Kong, People's Republic of China. [2]Irreversible Climate Change Research Center, Yonsei University, Seoul, South Korea. [3]Department of Atmospheric Sciences, Yonsei University, Seoul, South Korea. [4]Division of Environmental Science and Engineering, Pohang University of Science and Technology, Pohang, South Korea. [5]Climate and Environmental Research Institute, Korea Institute of Science and Technology, Seoul, South Korea. [6]Department of Atmospheric Sciences, University of Washington, Seattle, WA, USA. ✉email: sian@yonsei.ac.kr

npj

previous studies pointed out that the variability of the NAO is often underestimated in coupled climate models[36,72,73] and the heat flux forcing from the NAO to the sea surface may not be well-represented over the deep water formation region[55]. Also, the influence of the NAO on the AMOC via the Nordic Sea deep water formation can depend on the model's ability to represent the Nordic Sea–Atlantic Ocean exchange (e.g., through the Greenland–Scotland ridge overflow)[64,74]. Yet, the source of the intermodel diversity in the NAO–AMOC relationship has not yet been fully understood. In particular, the roles of oceanic processes and mean states have not been examined.

To understand why the decadal variability of the AMOC associated with the NAO differs widely in the coupled models, we analyzed preindustrial runs made with state-of-the-art CGCMs that participated in Coupled Model Intercomparison Project phase 6 (CMIP6; Table 1). Specifically, we thoroughly examined possible physical factors that could be responsible for different NAO–AMOC relationships between models, such as differences in NAO forcing or AMOC responsiveness. We show that the diverse NAO–AMOC relationships in the CGCMs are primarily shaped by oceanic mean states, which determine the sensitivity of the AMOC response to the surface buoyancy forcing induced by the NAO.

RESULTS

Large intermodel diversity of the NAO–AMOC relationship in CMIP6

The influence of the NAO on ocean circulation manifests itself through surface fluxes. During the positive phase of the NAO, anomalous westerly winds recurring in the SPNA provide a negative surface heat and freshwater fluxes to the ocean surface; these winds yield increases in seawater density and the strengthening of deep water formation in the SPNA, which is known to be closely related to the AMOC intensity[75–78]. Thus, a positive NAO tends to be followed by a strong AMOC. This relationship is evaluated using lagged regression coefficients between smoothed NAO and AMOC indices (β_τ where τ indicates lag). The observed NAO index can be measured as the difference between zonally averaged sea level pressure (SLP) at two latitudes during winter, with the SLP normalized at each latitude before subtracting[36] (Methods). In Fig. 1a (inset), its temporal relationship with various AMOC indicators, which are derived from the SST, salinity, and subsurface temperature[28,79–82] (for details, see Methods and Supplementary Fig. 1), is assessed. Although these indirect indicators do not directly represent the AMOC intensity and bear some uncertainties, being influenced by other local/remote factors[83–87], the consistency among them suggests a significant lead of the NAO over the AMOC. Previous study[88] has also reported a similar relationship in the observation where a positive NAO leads warm North Atlantic SST at the decadal timescale, which is thought to be made via heat transport of the AMOC. With the AMOC index for climate models defined as the maximum streamfunction at 40°N (Methods), most models except for 13 out of 42 reproduced a similar temporal relationship between the smoothed NAO and AMOC indices with a positive peak occurring at negative lags ('+NAO leading +AMOC' in Table 1; see Supplementary Fig. 2). The time lag is generally shorter in models compared to what is inferred from AMOC proxies. This could partly be attributed to the underestimation of the characteristic timescale of the NAO, indicated by significant peaks of power spectrums of the observed and simulated NAO indices (not shown). Another notable feature in the proxy-based relationship (Fig. 1a, inset) is significant negative peaks that tend to occur at positive lags, which is not simulated in CMIP6 models (discussed later). While the qualitative feature of a positive relationship where the NAO leads are largely consistent, the sensitivity of the AMOC to the NAO, which is assessed by the peak

magnitude of β_τ (hereafter, β, the value assessed within lag -10 to 0 years), differs greatly between the models (Fig. 1a). This shows that in CMIP6, significant intermodel diversity exists. Such diverse patterns have also been found in the coupled models of the CMIP phase 5 (CMIP5) generation[55]. However, for ocean-only models with the prescribed atmospheric forcing, the NAO's influence on the AMOC was robustly simulated across models[55].

Strong mean state-dependency of β

Figure 1b shows that the sensitivity of the AMOC to NAO (β) strongly depends on the mean characteristics of the SPNA (65°W–0°, 45°–63°N; hatched area in Fig. 2b), especially on the mixed layer depth (MLD) averaged over the strong-convection (FMA) season. Here, although both SPNA and Nordic Seas are known to be major deep water formation regions, in this study, we focus on the SPNA only because the NAO's influence on each region is known to be different[64] and the detailed physical processes in the Nordic Seas may be significantly model-dependent under the influence of overflows[64,74]. Among the 42 CMIP6 models, 39 (except INM-CM4–8, INM-CM5-0, and MIROC-ES2L) provided the MLD as an output variable, and it was found that the larger AMOC response tended to be induced by the NAO when the SPNA MLD was deeper on average. The correlation between the two is remarkably high ($r = 0.76$, black line), indicating that the mean SPNA MLD explains 58% of the variability of β. Although this high correlation value is to some extent attributable to the two models with the deepest mean MLD (GISS family), the correlation when excluding these two models ($r = 0.51$) still remains statistically significant at the 95% confidence level, indicating a robust relationship between the mean MLD and β. In other words, the diverse NAO–AMOC relationships in the CMIP6 models are closely related to diversity in the mean state of the SPNA. Note that no such relationship was found when the same analyze was conducted for the Nordic Seas (20°W–10°E, 65°–80°N, Supplementary Fig. 3).

Physical relationship between MLD and β

To understand the physical factors underlying the strong MLD dependency in the NAO–AMOC relationship in CMIP6, we first examined wintertime sea ice concentration (SIC) over the SPNA. In Fig. 2a, the mean SICs for each model are shown in descending order. Here, we divided the CMIP6 models into three groups based on this result (i.e., Groups 1, 2 and 3 in Fig. 2a). The criterion for dividing Group 1 and 2 is 15%, which is the value conventionally used when defining the sea ice extent (SIE). Group 3 was defined due to data availability, not for a physical reason, so we do not conduct separate analysis on Group 3. For Group 1, the sea ice during winter extends so far southeast that it covers a wide area in the SPNA (Fig. 2b). As this sea ice cap prevents surface flux anomalies from being delivered to the ocean, the mean MLD remains shallow, and the sensitivity of the AMOC to the NAO also decreases. Therefore, the Group 1 models are in the regime of shallow mean MLD and low β in Fig. 1b (open circles). Note that the eleven models in Group 1 do not necessarily share the same ocean component (ICON-O for ICON-ESM-LR, NEMO3.4.1 for the CanESM family, MPAS-Ocean for the E3SM family, and NEMO3.6 for the EC-Earth3 family and IPSL-CM6A-LR; Table 1). Although the mean SIE is rather large in Group 1 models, we cannot conclude that this is unrealistic, since the simulated mean field in this study represent the preindustrial condition whose atmospheric greenhouse gas concentration was lower. In fact, some of Group 1 models (E3SM-1-0, EC-Earth3-Veg, and CanESM5) have a relatively high climate sensitivity compared to others[89], which could have contributed to the colder mean state in the North Atlantic in the preindustrial simulation.

The second group consisted of the models that simulated smaller sea ice extent. While the cause of the low β in Group 1 can

Table 1. CMIP6 model configurations and classification based on the temporal relationship between the NAO and AMOC.

NAO–AMOC temporal relationship	Model	Atmospheric resolution	Oceanic resolution	Ocean component	Data length (yr)	Reference
+NAO leading + AMOC	ACCESS-CM2	1.9° × 1.3°	1° × 1°	MOM5	500	Dix et al.[121]
	ACCESS-ESM1-5	1.9° × 1.2°	1° × 1°	MOM5	900	Ziehn et al.[122]
	CMCC-ESM2	1.3° × 0.9°	1° × 0.6°	NEMO3.6	250	Lovato et al.[123]
	CMCC-CM2-SR5	1.3° × 0.9°	1° × 0.6°	NEMO3.6	500	Lovato et al.[124]
	CNRM-CM6-1	1.4° × 1.4°	1° × 0.6°	NEMO3.6	500	Voldoire[125]
	CNRM-CM6-1-HR	0.5° × 0.5°	0.25° × 0.17°	NEMO3.6	300	Voldoire[126]
	CESM2	1.3° × 0.9°	1° × 1°	POP2	1200	Danabasoglu et al.[127]
	CESM2-FV2	1.9° × 2.5°	1° × 1°	POP2	500	Danabasoglu et al.[128]
	CESM2-WACCM	1.3° × 0.9°	1° × 1°	POP2	499	Danabasoglu et al.[129]
	CESM2-WACCM-FV2	1.9° × 2.5°	1° × 1°	POP2	500	Danabasoglu et al.[130]
	E3SM-1-0	1° × 1°	1° × 1°	MPAS-Ocean	500	Bader et al.[131]
	E3SM-1-1	1° × 1°	1° × 1°	MPAS-Ocean	165	Bader et al.[132]
	FGOALS-g3	1° × 0.8°	1° × 1°	LICOM3	500	Li et al.[133]
	GISS-E2-1-G	2.5° × 2°	1.25° × 1°	GISS Ocean	345	NASA/GISS[134]
	GISS-E2-2-G	2.5° × 2°	1.25° × 1°	GISS Ocean	151	NASA/GISS[135]
	HadGEM3-GC31-LL	1.9° × 1.3°	1° × 0.5°	NEMO3.6	500	Ridley et al.[136]
	HadGEM3-GC31-MM	0.8° × 0.5°	0.3° × 0.1°	NEMO3.6	500	Ridley et al.[137]
	IPSL-CM6A-LR	2.5° × 1.25°	1° × 0.5°	NEMO3.6	800	Boucher et al.[138]
	MIROC6	1.4° × 1.4°	1° × 1°	COCO4.9	500	Tatebe and Watanabe[139]
	MIROC-ES2L*	2.8° × 2.8°	1° × 1°	COCO4.9	500	Hajima et al.[140]
	MPI-ESM-1-2-HAM	1.9° × 1.9°	1.5° × 1.5°	MPIOM1.6.3	780	Neubauer et al.[141]
	MPI-ESM1-2-HR	0.9° × 0.9°	0.4° × 0.4°	MPIOM1.6.3	500	Jungclaus et al.[142]
	MPI-ESM1-2-LR	1.9° × 1.9°	1.5° × 1.5°	MPIOM1.6.3	1000	Wieners et al.[143]
	MRI-ESM2-0	1.1° × 1.1°	1° × 0.5°	MRI.COM4.4	701	Yukimoto et al.[144]
	NorCPM1	1.9° × 1.9°	1° × 1°	MICOM	500	Bethke et al.[145]
	NorESM2-LM	2.5° × 1.9°	1° × 1°	MICOM	501	Seland et al.[146]
	NorESM2-MM	1.25° × 0.9°	1° × 1°	MICOM	500	Bentsen et al.[147]
	UKESM1-0-LL	1.9° × 1.3°	1° × 0.5°	NEMO3.6	1880	Tang et al.[148]
	UKESM1-1-LL	1.9° × 1.3°	1° × 0.5°	NEMO3.6	462	Mulcahy et al.[149]
+NAO co-occurring with + AMOC	CanESM5	2.8° × 2.8°	1° × 1°	NEMO3.4.1	1000	Swart et al.[150]
	CanESM5-CanOE	2.8° × 2.8°	1° × 0.6°	NEMO3.4.1	501	Swart et al.[151]
	EC-Earth3-LR	1.1° × 1.1°	1° × 0.6°	NEMO3.6	201	EC-Earth Consortium[152]
	ICON-ESM-LR	1.9° × 1.9°	0.4° × 0.4°	ICON-O	500	Lorenz et al.[153]
	INM-CM4-8*	2° × 1.5°	1° × 1°	INM-OM5	531	Volodin et al.[154]
	INM-CM5-0*	2° × 1.5°	0.5° × 0.25°	INM-OM5	1201	Volodin et al.[155]
Statistically not distinguished from zero[a]	CNRM-ESM2-1	1.4° × 1.4°	1° × 0.6°	NEMO3.6	500	Seferian[156]
	E3SM-1-1-ECA	1° × 1°	1° × 1°	MPAS-Ocean	165	Bader et al.[157]
	EC-Earth3	0.7° × 0.7°	1° × 0.6°	NEMO3.6	501	EC-Earth Consortium[158]
	EC-Earth3-AerChem	0.7° × 0.7°	1° × 0.6°	NEMO3.6	501	EC-Earth Consortium[159]
	EC-Earth3-CC	0.7° × 0.7°	1° × 0.6°	NEMO3.6	505	EC-Earth Consortium[160]
	EC-Earth3-Veg	0.7° × 0.7°	1° × 0.6°	NEMO3.6	500	EC-Earth Consortium[161]
	EC-Earth3-Veg-LR	1.1° × 1.1°	1° × 0.6°	NEMO3.6	501	EC-Earth Consortium[162]

Asterisk (*) represents models for which the MLD variable was not available at the time of analysis.
[a]With 'zero' referring to the lagged regression coefficient between the NAO and AMOC (Supplementary Fig. 2).
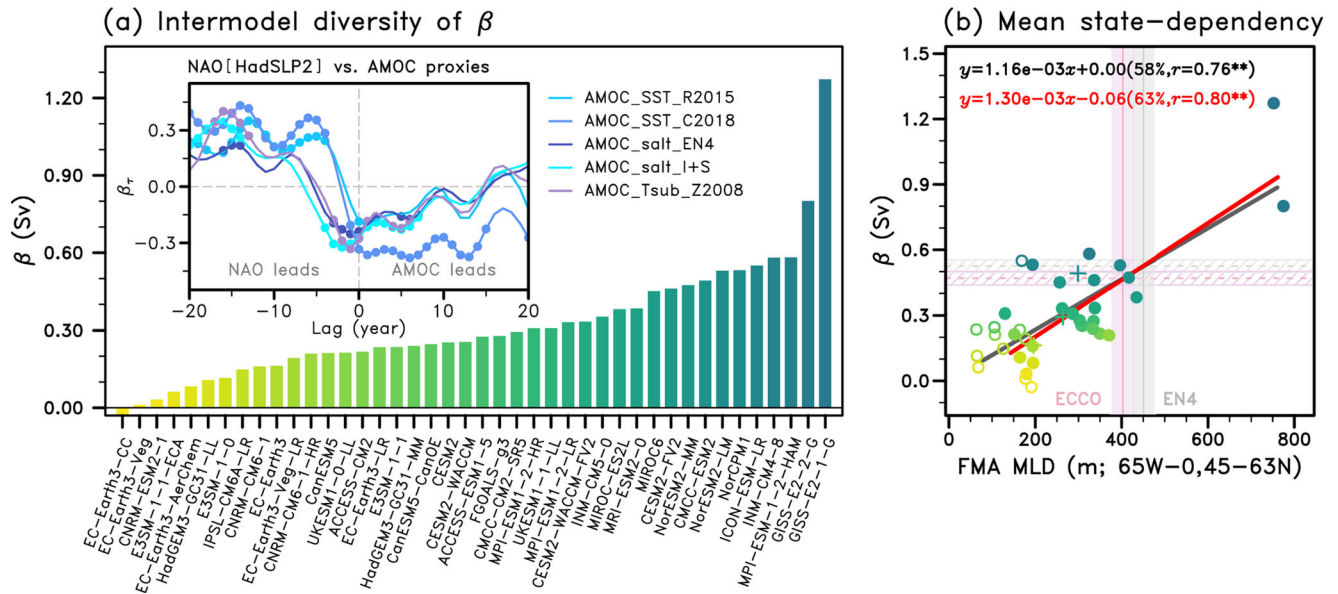
(a) Intermodel diversity of β

(b) Mean state-dependency

Fig. 1 Simulated/Estimated NAO–AMOC relationships and their mean state dependency. a The maximum regression coefficients (β; unit: Sv; $1\,Sv = 10^6\ m^3\ s^{-1}$) when the NAO leads the AMOC by less than 10 years for each model (both 5-year filtered; see Methods and Supplementary Fig. 2). The inset shows lagged regression coefficients (β_τ; unitless) of various AMOC indicators on the observed NAO index where τ indicates a lag (Methods). **b** A scatterplot of FMA-season climatological mean SPNA MLD (unit: m) and β. Color code for individual models follows that of (**a**). Regression slope for all available models is shown in black, and red is for Group 2 (closed circles) only. Open circles and crosses are for Group 1 and 3. The equations at the top left correspond to each regression line that has the same color. In the parenthesis, the goodness of fit (R^2; in %) and the Pearson correlation coefficient (r) are shown. The range of observed/observation-constrained MLD (Methods) is shown by vertical solid line with a 95% confidence interval (shaded). Based on the established relationship from CMIP6 (black line and equation), β is estimated for the observed MLD (dashed line and hatched area); gray for EN4 and pink for ECCO datasets. The bold dots in the inset of (**a**) and the asterisk symbol '**' in (**b**) indicate statistically significant values at the 95% confidence level, which was evaluated using a two-tailed Student's t test. In the inset, the effective sample size was considered (Methods).

be easily understood through the sea ice cover effect, it is not straightforward why β is proportional to the mean MLD within Group 2 ($r = 0.80$, red line in Fig. 1b). The low sea ice concentrations and open sea surface in SPNA during winter in Group 2 (Fig. 2c and Supplementary Fig. 4) are a prerequisite for high β, but not a direct cause. The mean SIC is significantly correlated with the magnitude of β in Group 2 ($r = -0.47$). However, this relationship becomes insignificant when excluding one outlier of GISS-E2-1-G ($r = -0.31$). Thus, the strong proportionality between the MLD and β within Group 2 indicates that factors other than the sea-ice cap affect the NAO–AMOC relationship. Considering that Group 3 models (Fig. 1b, cross marks) lie well within the range where Group 2 models are located and tend to have larger β as the mean MLD is deeper, it is also likely that the same underlying physical mechanism may be applicable for Group 3.

Given that the MLD is defined based on the vertical density gradient, the ocean stratification is a possible candidate for why the MLD and β are closely related. A relatively shallow average MLD in a model indicates strong stratification. The high vertical stability in the strongly stratified models inhibits the cross-isopycnal exchange of seawater, making the lower layer insensitive to surface processes. In contrast, models with a deeper average MLD, by definition, tend to be weakly stratified. Presumably, the weak vertical stability in these models easily permits deep sinking when surface water is densified, producing a deeper water mass. In other words, under the same buoyancy loss at the surface, deep water formation is induced more effectively by convection as the ocean column is more weakly stratified[65,90]. Thus, when negative buoyancy forcing is applied over the SPNA surface in association with a positive NAO, AMOC strengthening can be more effectively induced in weakly stratified models.

In Fig. 3a, b, we evaluate the relationship between the mean stratification and the sensitivity of the deep water formation to the

surface flux in CMIP6. In particular, given that deep convection by buoyancy loss of the surface water is a key process in maintaining the AMOC, we focus on the role of the surface buoyancy flux (i.e., heat and freshwater fluxes; Methods). The sensitivity of the deep water formation rate to the buoyancy flux (γ) was quantified for wintertime as the regression slope of anomalous MLD on the surface buoyancy flux, namely, on the effect of heat flux (γ_H) and freshwater flux (γ_F), separately. Here, among the components that constitute freshwater flux into the SPNA, that from runoff tends to be one order smaller in its magnitude compared to the net precipitation (precipitation minus evaporation [P−E]; not shown), so we do not consider the runoff effect. For the same reason and the sake of simplicity, we do not take sea ice effect into account, although its close location to the deep water formation region may have some role. Figure 3a, b show that in Group 2 (red slopes), when the model has a deeper climatological mean MLD, the magnitude of γ tends to become larger for both types of surface buoyancy forcing, indicating that the effect of the NAO can be better transmitted to the AMOC (i.e., a higher β for larger negative γ; Fig. 3c, d and schematically shown in Fig. 5). At first glance, both the mean MLD and β seem more strongly linked to γ_H than to γ_F, judging by their correlation coefficients (for example, the correlation of the MLD with γ_H is $r = -0.75$ for Group 2, which is larger in its magnitude than $r = -0.61$ of that with γ_F). However, we find no statistically significant difference, making it difficult to conclude the relative importance of heat and freshwater fluxes in shaping the intermodel diversity.

The role of NAO forcing

Now, we examine the possible contributions of NAO forcing to the wide intermodel spread of β. In previous studies, it has been considered that the inherent characteristics of the NAO in each model, such as the magnitude of its amplitude[36,72] or how the
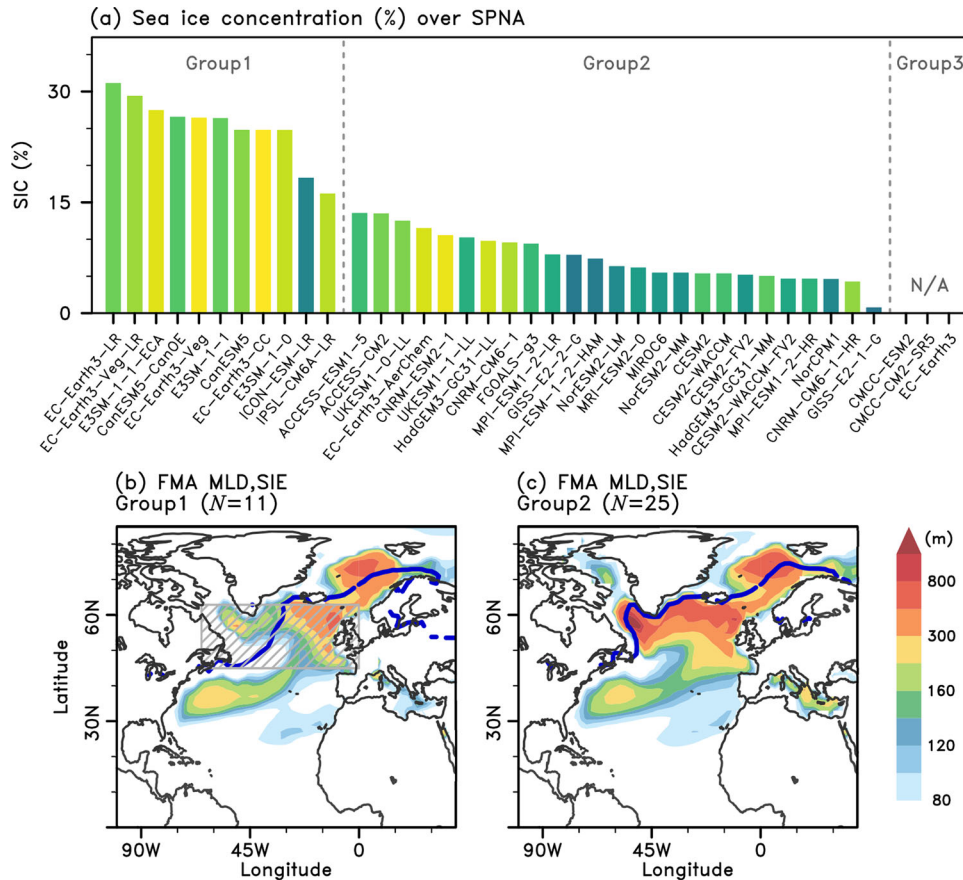
Fig. 2 FMA-mean characteristics in the SPNA and the North Atlantic. a Sea ice concentration (SIC; unit: %) averaged over the SPNA region (hatched area in **b**) for each model where color code for individual models follows that of Fig. 1a. Models are arranged by descending order of the SPNA-averaged SIC. Gray vertical line divides each group. For three models in Group 3, the SIC variable was not available (N/A). **b, c** Ensemble mean of FMA-mean mixed layer depth (shaded; unit: m) and SIE outline (dark blue line) for each group. The number of models used for each group is shown as N. Here, SIE was defined as the boundary of the region where the sea ice concentration is maintained larger than 15%. Individual model results are shown in Supplementary Fig. 4.

associated surface flux pattern is simulated[55] are related to the different NAO–AMOC relationships in CGCMs. If the NAO amplitude is a critical factor in shaping the NAO–AMOC relationship in climate models, the larger the amplitude of the NAO forcing, the stronger its influence on the AMOC (i.e., higher β). To examine whether such relationship exists for CMIP6 models, we measure the NAO amplitude as the contrast of between maximum and minimum pressure anomalies that is induced by the NAO in the North Atlantic (see Methods). However, Fig. 4a shows that there was no significant relationship between β and NAO amplitude at the decadal timescale. Similar analysis was repeated with unsmoothed NAO index (Supplementary Fig. 5) and again, no significant contribution of the NAO amplitude to β was found. We also investigated a different definition of the NAO amplitude: the standard deviation of the zonal mean SLP differences at each latitude (without normalizing). In this case as well, the interannual or low-frequency variability of the NAO was not a good predictor for β ($r = -0.21$ and -0.25, respectively, both not statistically significant). Thus, we conclude that the NAO amplitude is unlikely to be a major factor in shaping different NAO–AMOC relationships between CMIP6 models. It is also worth discussing that in Fig. 4a, 20 out of 42 models simulated the decadal variability of the NAO close to the observed value (8.415, the bias being less than 5%), which is located exactly at median (i.e., 21 models simulate smaller values than the observation, and 21 models simulate larger values). This differs from previous studies that reported underestimation of low-frequency variability of the NAO in climate

models[36,72,73], which may be attributed to differences in a generation of models (i.e., CMIP5 and CMIP6) and/or a definition of the NAO amplitude.

Another possible contributor to diverse NAO–AMOC relationships is the spatial pattern of the surface flux forcing induced by the NAO. Although CMIP6 models generally well-reproduce the dipole structure of the NAO (Supplementary Fig. 6), the detailed spatial feature somewhat differs between models, being consistent with a previous study that used the CMIP5 models[91]. It further leads to different surface flux forcing patterns to the SPNA surface (Supplementary Figs. 7, 8). Xu et al.[55] showed that in a coupled model in which the NAO does not induce significant heat flux anomalies in the deep water formation region, the NAO–AMOC relationship is not well-simulated. We also found that in Group 1, the region where the NAO induced significant heat and freshwater flux anomalies tended to be inconsistent with the climatological deep-convection site (Supplementary Figs. 7, 8). Thus, the spatial pattern of NAO forcing, in addition to the insulation created by the sea ice, contributed to the weak influence of the NAO on the AMOC in Group 1. Similarly, in the three models in Group 2 (ACCESS-CM2, ACCESS-ESM-1-5, and CNRM-ESM2-1) that simulate low β, the NAO forcing region does not match the deep water formation region well. However, in most of the Group 2 models (22 out of 25), the regions of significant NAO forcing and that of deep water formation are generally co-localized. Therefore, how well the surface flux pattern is overlapped with the deep water
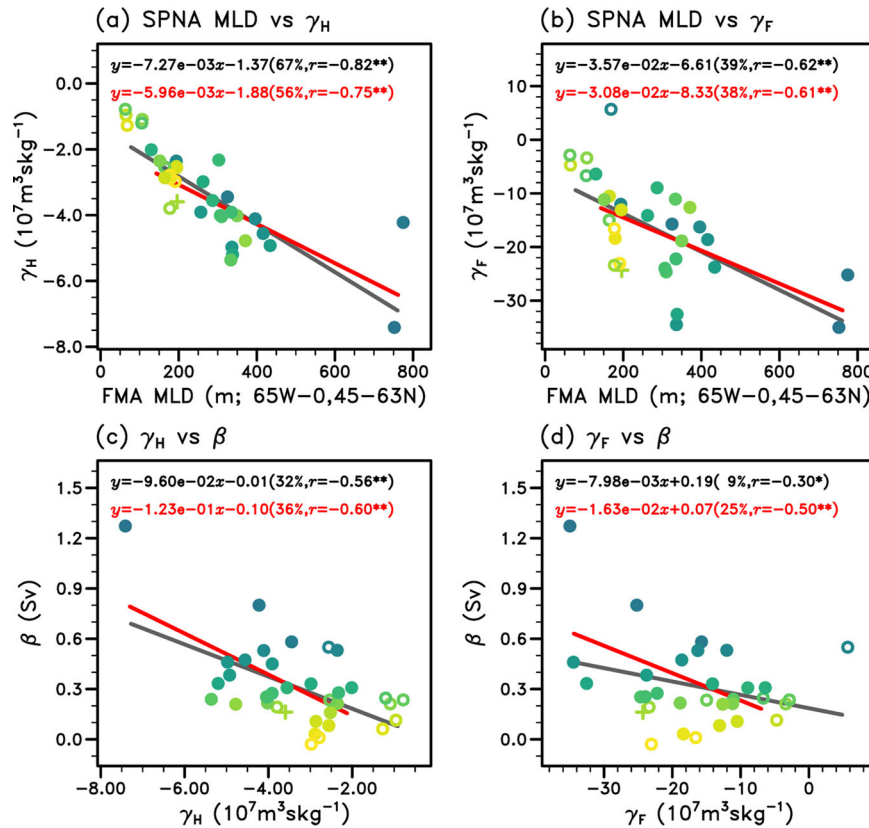
Fig. 3 Effect of mean stratification on γ and β. a, b Scatterplots of FMA climatological mean SPNA MLD (unit: m) and γ (a measure of the sensitivity of the deep water formation rate to each surface flux) with color code for individual models following that of Fig. 1a; (**a**) for buoyancy flux by heat (γ_H; unit: kg m^{-2} s^{-1}), and (**b**) for buoyancy flux by freshwater (γ_F; unit: kg m^{-2} s^{-1}). (**c**) and (**d**) show γ_H and γ_F against β. Without an outlier (GISS-E2-1-G) in (**c**), the correlation is -0.35, which is significant at the 95% confidence level. The notation of lines and equations follows that of Fig. 1b. Among 42 CMIP6 models, 36 models provided all variables required for (**a**) and (**c**) (MLD, heat flux, SLP, and oceanic streamfunction) except CMCC-ESM2, CMCC-CM2-SR5, INM-CM4-8, INM-CM5-0, IPSL-CM6A-LR, and MIROC-ES2L. For (**b**) and (**d**) where freshwater flux is required, 32 models were used except CNRM-CM6-1, E3SM-1-1-ECA, FGOALS-g3, and MIROC6 in addition to the above. Asterisk symbols '*' and '**' indicate statistically significant values at the 90% and 95% confidence level, respectively.

formation region can explain the diverse NAO–AMOC relationships only in a limited manner, particularly for models with low β.

Furthermore, we quantitatively examined the effect of the NAO's efficiency in inducing the buoyancy flux anomaly in the SPNA, as the regression slope (α) of the SPNA-averaged buoyancy flux anomalies onto the NAO index. Again, both heat and freshwater fluxes were considered by α_H and α_F. The relationships between α and β (Fig. 4b, c) suggest that the stronger the surface buoyancy flux induced by the NAO (large negative α), the greater the sensitivity of the AMOC to the NAO (high β) when all models are considered (black lines). This relationship partly depends on the small α and low β of Group 1 (open circles), which arise from the sea ice cover effect. The relationship between α and β within Group 2 is rather weak (red lines) and substantially affected by a single extreme case (GISS-E2-1-G). Without GISS-E2-1-G, neither α_H nor α_F significantly contributes to the β diversity ($r = -0.15$ and $r = -0.24$, respectively). Therefore, we conclude that the β diversity is to some extent physically related to the synchronicity between the NAO forcing and deep water formation regions and the surface forcing efficiency of the NAO, but they are not likely to be a direct factor to determine β, particularly in Group 2.

DISCUSSION

Through the analyses above, it has been shown that the spread of β in CMIP6 is strongly linked to how the mean climate states are simulated; if the sea ice extends too far to cover the SPNA or the upper-level ocean stratification in the SPNA is strong, the surface

forcing caused by the NAO does not effectively lead to AMOC change. On the other hand, if the SPNA surface remains open during winter and the oceanic stratification is relatively weak, the NAO forcing easily perturbs the deep water formation rate of the AMOC, yielding a positive relationship where the NAO leads the AMOC. This implies that if the average oceanic state is similar between the models, the influence of the NAO on the AMOC variability is also expected to be similar. Indeed, for ocean-only models whose mean states are less diverse (e.g., comparing Fig. 13 of Danabasoglu et al.[92] and Supplementary Fig. 4), the relationship where the NAO leads the AMOC is consistent among these models[55]. The small diversity in ocean models further suggests that differences in model configurations (e.g., parameterization schemes for vertical mixing) have a relatively minor effect on the intermodel spread when they are not coupled to atmospheric models. That is, the atmosphere–ocean feedback processes in CGCMs are likely the key factor that enables small biases to grow and constitute the different oceanic mean states in the SPNA across models, and hence, the NAO–AMOC relationship. In ocean-only models, as the prescribed atmospheric field lowers the degree of freedom, prohibiting the two-way interaction between the atmosphere and ocean, oceanic states appear less diverse.

So far, the influence of the NAO on the AMOC has been investigated for a decadal and longer timescale, from which a further question may be raised: where does atmospheric low-frequency (annual and longer) variability come from? Previous studies have proposed evidence of oceanic influence on the Atlantic atmospheric variability based on climate models. For

example, Wen et al.[54] and Gastineau and Frankignoul[93] suggested that changes in the NAO could be driven by the internal variability of ocean circulation. Msadek and Frankignoul[94] and Sun et al.[45] suggested a coupled atmosphere–ocean variability, where the atmosphere-induced AMOC change feeds back the atmosphere through meridional heat transport and sea surface warming using IPSL-CM4 and CCSM3 climate models, respectively. For the estimated result for the observation (Fig. 1, inset), the negative peaks of the NAO–AMOC relationship, when the AMOC proxies lead the NAO, imply the possibility for such a coupled mode to operate in situ. In CMIP6, on the other hand, the AMOC influence on the NAO (i.e., correlations when the AMOC leads) is somewhat unclear and depends on the model (Supplementary Fig. 2), suggesting that the feedback from the AMOC to the NAO is weak or absent in most models. Since fast response of the atmosphere to the ocean forcing may be more notable at the interannual timescale (i.e., without applying a low-pass filter), we also investigated the influence of the AMOC on the NAO using raw annual time series. However, no clear evidence of coupled mode was found (not shown). Therefore, further investigation at an individual model level is required to identify how NAO variability is affected by oceanic processes in the CMIP6 models.

SUMMARY AND IMPLICATIONS

It is thought that to improve climatic predictions in the Northern Hemisphere, climate models should be capable of simulating the NAO–AMOC relationship[36]. This is because the AMOC fluctuation, which significantly modulates the North Atlantic surface temperature, can be driven by changes in the NAO. The NAO–AMOC relationship was robustly simulated in ocean-only models when NAO-type atmospheric forcing was prescribed; however, this was not the case in fully coupled models where the models were allowed to resolve two-way air–sea feedback. This study thus attempted to determine what causes inconsistent, different NAO–AMOC relationships in coupled models based on a quantitative comparison, and to provide hints for a better simulation of AMOC variability. As a result, we found that models with a deep SPNA MLD tend to simulate the high sensitivity of the AMOC to the NAO. This relationship is related to two important factors: (i) the sea-ice cover effect in shallow-MLD models and (ii) the high sensitivity of deep convection to surface buoyancy forcing in deep-MLD models. Judging from the difference between ocean-only models and coupled models, the diverse mean MLDs in the SPNA can further be attributed to the two-way interaction between the atmospheric and oceanic fields. The above processes are schematically illustrated in Fig. 5.

These results provide valuable insights into decadal climate predictions. First, they emphasized that the key to improving the NAO-related AMOC variability in climate models (ultimately, to help improving the predictability of the northern hemisphere surface climate) might lie in the intermediate process by which the NAO signal is delivered to the AMOC, and it may eventually be achieved by reducing biases in the mean state. This result is different from ones brought forth by previous studies that focused more on the role of NAO forcing. Nevertheless, our results do not completely rule out this established viewpoint, as the NAO forcing pattern and efficiency also contribute to the β diversity to some extent. Second, the strong mean-state dependency of β provides some potential for using the observed NAO index to estimate AMOC strength for the next decade. Here, while β itself does not provide detailed information of time lag (which instead, can be inferred from the relationship between the observed NAO and AMOC proxies in Fig. 1a, inset), it can be used to estimate the magnitude of the AMOC change. The CMIP6-based regressive relationship implies an AMOC sensitivity of 0.53 (0.47) Sv per unit NAO change for the observed MLD of 450.30 (402.44) m in the EN4 (ECCO) dataset (Fig. 1b and Methods). It is also noteworthy
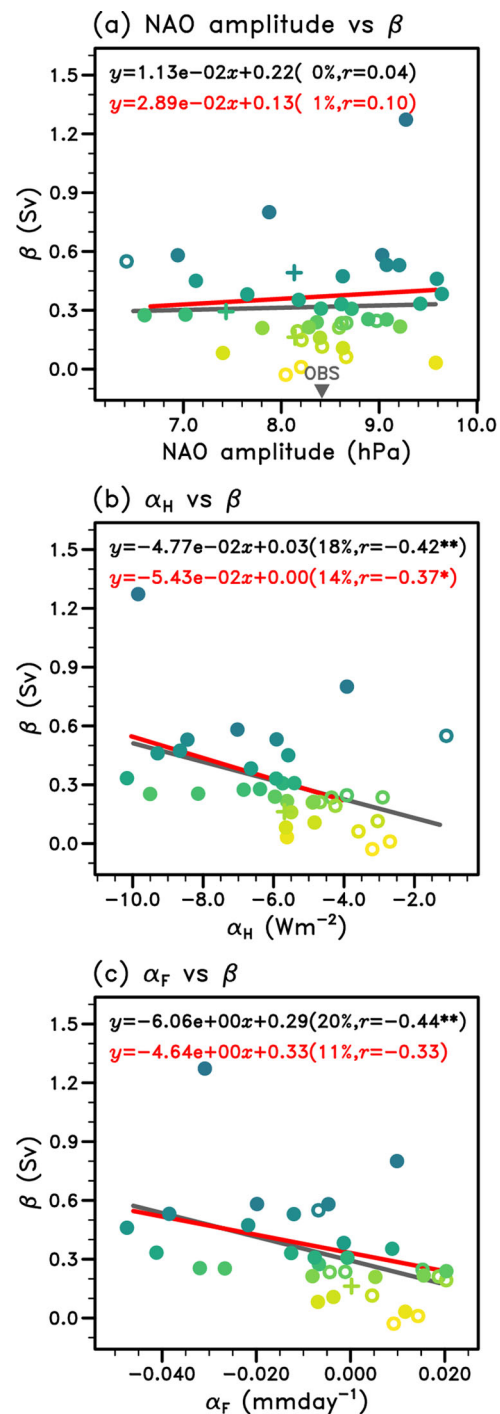

Fig. 4 Role of the NAO forcing in β diversity. a Scatterplot of the amplitude (unit: hPa; see Methods for the definition) of decadal NAO forcing and β (unit: Sv) with color code for individual models following that of Fig. 1a. **b, c**: as in (**a**), but for α_H (unit: W m^{-2}) and α_F (unit: mm day^{-1}) on the x-axis. α_H and α_F are used as a measure of the NAO efficiency to induce surface heat and freshwater flux at decadal timescale, respectively. The notation of lines and equations follows that of Fig. 1b. The qualitative results are insensitive to the window length. Among 42 CMIP6 models, 36 models provided all variables required for (**a**) and (**b**) (heat flux, SLP, and oceanic streamfunction) except CMCC-ESM2, CMCC-CM2-SR5, INM-CM4-8, INM-CM5-0, IPSL-CM6A-LR, and MIROC-ES2L. For (**c**) where freshwater flux is required, 32 models were used except CNRM-CM6-1, E3SM-1-1-ECA, FGOALS-g3, and MIROC6, and MIROC-ES2L. Asterisk symbols '*' and '**' indicate statistically significant values at the 90% and 95% confidence levels, respectively.
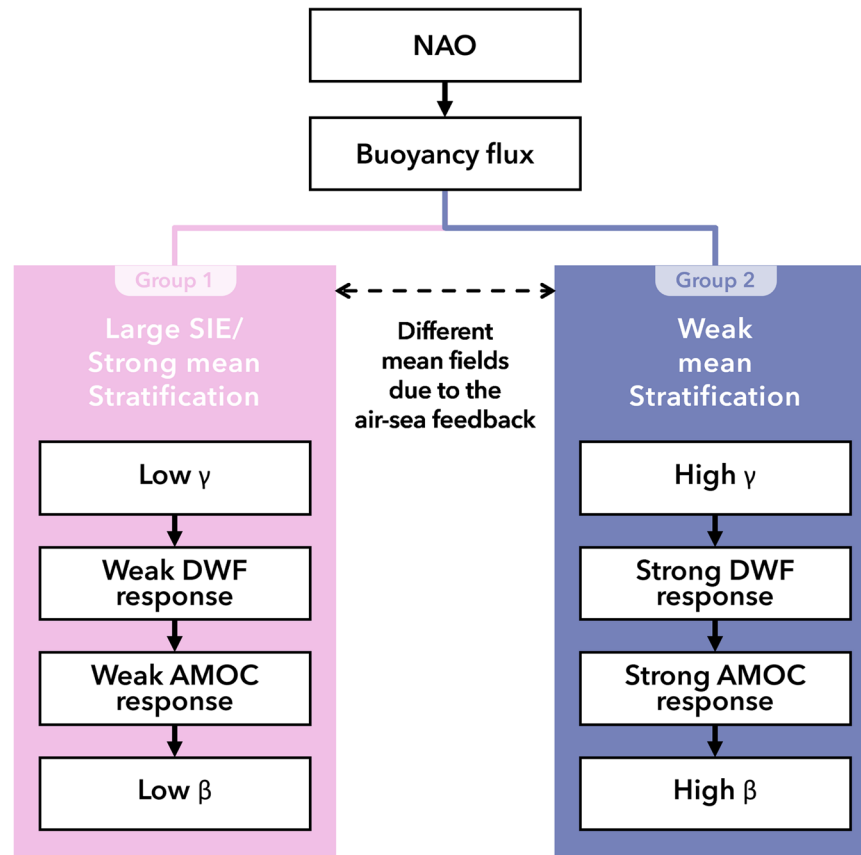
Fig. 5 Schematic representation of NAO influence on the AMOC for each group. This schematic illustrates why coupled climate models simulate different sensitivities of the AMOC to the NAO (β). Colored box indicates a group of models that share the similar background states; pink for Group 1 and blue for Group 2. 'SIE' means sea ice extent and 'DWF' represents deep water formation. See Text for more detailed illustration.

that CMIP6 models tend to underestimate the NAO influence on AMOC variability, given that the majority of the models (37 out of 42 models) underestimated the mean MLD. Finally, according to climate models, anthropogenic greenhouse gas warming is expected to strengthen oceanic stratification through surface heat and/or freshwater fluxes, shoaling the MLD[32,95–97]. Overall, this study suggests that the future AMOC is likely to be less sensitive to NAO change, providing important insights for decadal prediction under climate change. Indeed, Ma et al.[98] has reported a diminished relationship between the NAO and the AMOC in a greenhouse gas-forced simulation compared to the preindustrial, although a positive NAO induced negative AMOC in their study due presumably to the model-specific deep water formation site. It should also be noted that climate change modulates characteristics of the NAO and AMOC as well, such as their amplitude, frequency, and mean intensity[26,98–101], which will affect future NAO–AMOC interactions.

METHODS

Observational dataset
We used the Hadley Centre's monthly historical mean SLP dataset[102] (HadSLP2) for the NAO index and the monthly Extended Reconstructed Sea Surface Temperature version 4[103] (ERSST v4) for the SST-based AMOC indices for the period 1854–2015. For one of the salinity-based AMOC indices, the Hadley Centre EN4 dataset[104] (EN4) for the period 1950–2019. The other salinity-based index was obtained from a combination of two datasets, ISHII[105] and Scripps[106,107] (1945–2019) where the

ISHII data was used for the period before 2012, and the Scripps data for the subsequent period.

The MLD was retrieved from two datasets. One was derived using the oceanic temperature and salinity obtained from EN4. Because the vertical grid spacing becomes relatively coarse below 100 m, linear interpolation was first applied to the temperature and salinity at a 5-m interval. The potential density was then calculated, and the MLD was defined as the depth at which the potential density differed from the surface value by 0.125 kg m^{-3}. The other is the ECCO Version 4, Release 4 (v4r4)[108], which is a general circulation model (MITgcm) result constrained by satellite and in situ observations for the period 1992–2017. In this dataset, the MLD is defined using a different criterion; the depth at which the temperature differed from the surface value by 0.8 °C. Since no significant trend over time was found in the MLD derived from EN4 (which has a longer data length), we assume that the regression model obtained from CMIP6 preindustrial runs (Fig. 1b) can be employed for the more recent observation.

All observational data were linearly detrended at the beginning of any calculation to eliminate the effect of anthropogenic forcing and to focus on the natural variability.

Index definition
For the CMIP6 models, the AMOC index was defined as the maximum streamfunction at 40°N and below 500 m in the Atlantic basin[80]. A latitude of 40°N was chosen to focus on the specific process associated with the AMOC: sinking at high latitudes by deep water formation. It is also known that the AMOC definitions at lower latitudes tend to vary coherently with that at 40°N with time lag[109–111].

To estimate the observed AMOC intensity, five indirect AMOC indices were used because the data obtained via direct observation is insufficient (Supplementary Fig. 1 and inset of Fig. 1). The SST-based index of Ramhstorf et al.[28] (AMOC_SST_R2015) is defined as the difference of SST between the subpolar gyre region and the Northern Hemisphere by subtracting the latter from the former. By this, the temperature in the subpolar area, where changes in the ocean circulation leave their characteristic footprint on the sea surface[79], is isolated from the anthropogenically-induced large-scale temperature changes (represented by the Northern Hemisphere mean temperature). The subpolar gyre region was selected as the area whose linear trend of the SST is negative during the period 1880–2015[112]. The AMOC_SST_C2018 index is a modified version of AMOC_SST_R2015, developed by Caesar et al.[79] It is defined as the subpolar North Atlantic SST minus global mean SST during wintertime (November to May). The third and fourth indirect indices are derived from the salinity, using the same definition but different datasets. Based on the fact that the AMOC transports salty water from the subtropics to the subpolar region, they are defined as the integrated salinity in 0–1500 m and 45–65° N in the Atlantic[81]. The EN4 dataset (1950–2019) and ISHII and Scripps dataset (1945–2019) were used for AMOC_salt_EN4 and AMOC_salt_I + S, respectively. Finally, the fingerprint index of Zhang[80] (AMOC_Tsub_Z2008) is obtained from the first principal component of the leading mode of the annual mean subsurface (400 m) temperature using the EN4 temperature. This index reflects the realignment of the oceanic current system that involves northern recirculation gyre and western boundary currents with changes in the AMOC strength. All proxies are normalized to indicate whether the AMOC is in an anomalously strong or weak state (i.e. qualitative feature of temporal evolution of the AMOC) and to be compared with each other (Supplementary Fig. 1). Although these indirect AMOC indices were developed upon physical basis, it should be borne in mind that the SST and salinity as well as the subsurface temperature in the North Atlantic can also be modulated by other sources than the AMOC, such as external forcings[83,84,113–116] or forcings from other areas[85–87].

The observed/modeled NAO index was defined as follows. First, the correlations of zonally averaged sea level pressure (SLP; where $\overline{X}$ indicates the zonal mean of X) in the Atlantic basin (80°W–30°E) between any two latitudes were calculated; then, the two latitudes with the largest negative correlations were identified in each model or observation. The difference in the normalized SLP between those two latitudes was defined as the NAO index[36]. It represents the SLP contrast between the Subtropical (Azores) High and the Subpolar Low, and it is similar to the conventional station-based definition which is more widely used, except that the former is defined as the difference between two latitudes and the latter as the difference between the two points (Lisbon, Portugal and Stykkisholmur/Reykjavik, Iceland)[117]. The major difference in physical meaning is that the NAO definition used here considers the spatial structure of the NAO, which could depend on the individual model, instead of using fixed station points.

As NAO variability is known to be most pronounced during boreal winter, DJF-mean values are taken for all variables when conducting the regression analysis related to the NAO forcing.

NAO amplitude
The amplitude of a climate variability is often measured as the standard deviation of its index time series. However, since the above definition of the NAO index requires normalization at each latitude as a preprocess, the standard deviation of the final index does not appropriately represent the magnitude of variability of the NAO. Thus, as an alternative, we normalize the NAO index and regress the SLP anomalies at each grid point to it so that the regression slope represents the SLP anomaly (in hPa) induced by a unit NAO index change. Then, the difference between maximum and minimum SLPs in the North Atlantic, which are detected at the cores of high and low pressures systems, is defined as the NAO amplitude.

Quantitative evaluation of α, β, and γ
All variables were linearly detrended before the following analysis to avoid being affected by any model drift. The AMOC sensitivity to NAO (β) was measured based on linear regression analysis using

$$\text{AMOC}(t) = b_\tau + \beta_\tau \cdot \text{NAO}(t + \tau) \qquad (1)$$

where τ represents the time lag (years), and b_τ and β_τ indicate the y-intercept and slope corresponding to lag τ, respectively. To reflect the intrinsic timescale of the AMOC associated with its large inertia, the NAO and AMOC indices were smoothed using a 5-year low-pass Lanczos filter before calculating β_τ. The qualitative result (i.e., strong dependency of the NAO–AMOC relationship on the mean MLD; see Text) is not sensitive to the choice of window length or cutoff period. The results of β_τ for each model are shown in Supplementary Fig. 2 for a lag τ between −20 and 20 years (a negative value indicates that the NAO leads).

In general, there is qualitative agreement in CMIP6 models that a positive peak appears when the NAO leads or co-occurs with the AMOC, namely, between lag −10 and 0 (Supplementary Fig. 2). Considering that the AMOC index represents a basin-wide large-scale circulation rather than a local process, the exact locations of the peaks may depend on the model. Therefore, for a quantitative comparison between models, AMOC sensitivity to NAO (β) was defined as the maximum β_τ between lag −10 and 0. The results in Fig. 1a reveal a difference between the smallest (−0.029 Sv for EC-Earth3-CC) and the largest (1.273 Sv for GISS-E2-1-G) cases by two orders of magnitude.

Similarly, α and γ are measured as the regression slope as follows:

$$\text{Flux}(t) = a + \alpha \cdot \text{NAO}(t) \qquad (2)$$

and

$$\text{MLD}(t) = c + \gamma \cdot \text{Flux}(t) \qquad (3)$$

Here, Flux is the surface heat or freshwater flux from the atmosphere to the ocean, and a and c are the y-intercepts. The time lag is not considered when measuring α and γ, because interactions between the NAO and the surface fluxes and between the surface fluxes and the MLD are most efficient at lag 0.

Effective sample size of auto-correlated data
For the temporal correlated data such as low-pass filtered NAO/AMOC index in this study, its 'effective' sample size is less than the number of individual sample measurements (i.e., the number of time steps in time series). When evaluating the statistical significance of the correlation/regression coefficients between such auto-correlated two datasets with a raw sample size of N, the effective sample size (N_{eff}) can be taken into account by using the following formula[36,50,118]:

$$\frac{1}{N_{eff}} \approx \frac{1}{N} + \frac{2}{N} \sum_{j=1}^{N} \frac{N-j}{N} \rho_{xx}(j)\rho_{yy}(j) \qquad (4)$$

where $\rho_{xx}(j)$ and $\rho_{yy}(j)$ are the autocorrelations at lag j for each data x and y. With this effective sample size, we evaluated the statistical significance of regression slopes (α, β, and γ) using the two-tailed Student's t-test.

Buoyancy flux by heat and freshwater
To facilitate direct comparison of heat and freshwater effects on MLD deepening, we derived surface buoyancy flux by heat (B_h)

and by freshwater (B_w) using bulk formula[119] so that B_h and B_w have the same unit (kg m^{-2} s^{-1}). B_h and B_w are then substituted into Flux(t) when calculating γ. B_h is obtained from

$$B_h = \frac{a_h Q_{net}}{C_p} \tag{5}$$

where a_h and C_p are the thermal expansion coefficient (10^{-4} K^{-1}) and specific heat of the seawater (4000 J K^{-1} kg^{-1})[120], assumed to be constants for the sake of simplicity. Q_{net} is the net surface heat flux.

The buoyancy flux by freshwater flux (B_w) is given by

$$B_w = \beta_w \rho S(P - E) \tag{6}$$

Similarly, the haline contraction coefficient ($\beta_w = 8.0 \times 10^{-4}$ psu^{-1}), water density ($\rho = 1022.4$ kg m^{-3}), and the sea surface salinity ($S = 35$ psu)[120] are regarded as constants. P and E represent precipitation and evaporation, respectively.

DATA AVAILABILITY
All data used in this study can be retrieved from publicly available depositories: HadSLP2 from https://rda.ucar.edu/datasets/ds277.4/; ERSST v4 from https://psl.noaa.gov/data/gridded/data.noaa.ersst.v4.html; EN4 from https://www.metoffice.gov.uk/hadobs/en4/download.html; ISHII salinity from https://rda.ucar.edu/datasets/ds285.3/; Scripps salinity from https://argo.ucsd.edu/data/argo-data-products/; ECCO from https://cmr.earthdata.nasa.gov/virtual-directory/collections/C1990404819-POCLOUD/temporal; CMIP6 data from the Earth System Grid Federation (ESGF) nodes (https://esgf-data.dkrz.de/projects/esgf-dkrz/).

CODE AVAILABILITY
The source codes used in this study are available from the corresponding author upon reasonable request.

REFERENCES
1. Broecker, W. S. Thermohaline circulation, the Achilles heel of our climate system: Will man-made CO$_2$ upset the current balance? *Science* **278**, 1582–1588 (1997).
2. Broecker, W. S. Was a change in thermohaline circulation responsible for the Little Ice Age? *Proc. Natl Acad. Sci. USA* **97**, 1339–1342 (2000).
3. Clark, P., Pisias, N. G., Stocker, T. F. & Weaver, A. J. The role of the thermohaline circulation in abrupt climate change. *Nature* **415**, 863–869 (2002).
4. Maier, E. et al. North Pacific freshwater events linked to changes in glacial ocean circulation. *Nature* **559**, 241–245 (2018).
5. Stolpe, M. B., Medhaug, I., Sedlácek, J. & Knutti, R. Multidecadal variability in global surface temperatures related to the Atlantic meridional overturning circulation. *J. Clim.* **31**, 2889–2906 (2018).
6. Caesar, L., Rahmstorf, S. & Feulner, G. On the relationship between Atlantic meridional overturning circulation slowdown and global surface warming. *Environ. Res. Lett.* **15**, 024003 (2020).
7. Sutton, R. T. & Hodson, D. L. R. Atlantic Ocean forcing of North American and European summer climate. *Science* **309**, 115–118 (2005).
8. Goldenberg, S. B., Landsea, C. W., Mestas-Nuñez, A. M. & Gray, W. M. The recent increase in Atlantic hurricane activity: causes and implications. *Science* **293**, 474–479 (2001).
9. Yan, X., Zhang, R. & Knutson, T. R. The role of Atlantic overturning circulation in the recent decline of Atlantic major hurricane frequency. *Nat. Commun.* **8**, 1–7 (2017).
10. Gervais, M., Shaman, J. & Kushnir, Y. Impacts of the North Atlantic warming hole in future climate projections: Mean atmospheric circulation and the North Atlantic jet. *J. Clim.* **32**, 2673–2689 (2019).
11. Jackson, L. C. et al. Global and European climate impacts of a slowdown of the AMOC in a high resolution GCM. *Clim. Dyn.* **45**, 3299–3316 (2015).
12. Bjerknes, J. Atlantic air-sea interaction. *Adv. Geophys.* **10**, 1–82 (1964).
13. Donohoe, A., Marshall, J., Ferreira, D. & Mcgee, D. The relationship between ITCZ location and cross-equatorial atmospheric heat transport: from the seasonal cycle to the last glacial maximum. *J. Clim.* **26**, 3597–3618 (2013).
14. Schneider, T., Bischoff, T. & Haug, G. H. Migrations and dynamics of the intertropical convergence zone. *Nature* **513**, 45–53 (2014).
15. Kang, S. M. Extratropical influence on the tropical rainfall distribution. *Curr. Clim. Chang. Rep.* **6**, 24–36 (2020).
16. Parsons, L. A., Yin, J., Overpeck, J. T., Stouffer, R. J. & Malyshev, S. Influence of the Atlantic meridional overturning circulation on the monsoon rainfall and carbon balance of the American tropics. *Geophys. Res. Lett.* **41**, 146–151 (2014).
17. Sandeep, N. et al. South Asian monsoon response to weakening of Atlantic meridional overturning circulation in a warming climate. *Clim. Dyn.* **54**, 3507–3524 (2020).
18. Vellinga, M. & Wood, R. A. Global climatic impacts of a collapse of the Atlantic thermohaline circulation. *Clim. Change* **54**, 251–267 (2002).
19. Mohtadi, M. et al. North Atlantic forcing of tropical Indian Ocean climate. *Nature* **508**, 76–80 (2014).
20. Vikebø, F. B., Sundby, S., Ådlandsvik, B. & Otterå, O. H. Impacts of a reduced thermohaline circulation on transport and growth of larvae and pelagic juveniles of Arcto-Norwegian cod (Gadus morhua). *Fish. Oceanogr.* **16**, 216–228 (2007).
21. Edwards, M., Beaugrand, G., Helaouët, P., Alheit, J. & Coombs, S. Marine ecosystem response to the atlantic multidecadal oscillation. *PLoS ONE* **8**, 1–5 (2013).
22. Barange, M. et al. *Impacts of Climate Change on Fisheries and Aquaculture* (FAO Fisheries and Aquaculture Technical Paper, 2018).
23. Tourre, Y. M., Rousseau, D., Jarlan, L., Le Roy Ladurie, E. & Daux, V. Western European climate, and Pinot noir grape harvest dates in burgundy, france, since the 17th century. *Clim. Res.* **46**, 243–253 (2011).
24. Cheng, W., Chiang, J. C. H. & Zhang, D. Atlantic meridional overturning circulation (AMOC) in CMIP5 Models: RCP and historical simulations. *J. Clim.* **26**, 7187–7197 (2013).
25. Kim, H. & An, S.-I. On the subarctic North Atlantic cooling due to global warming. *Theor. Appl. Climatol.* **114**, 9–19 (2013).
26. Weijer, W., Cheng, W., Garuba, O. A., Hu, A. & Nadiga, B. T. CMIP6 models predict significant 21st century decline of the Atlantic Meridional Overturning Circulation. *Geophys. Res. Lett.* **47**, e2019GL086075 (2020).
27. Bryden, H. L., Longworth, H. R. & Cunningham, S. A. Slowing of the Atlantic meridional overturning circulation at 25° N. *Nature* **438**, 655–657 (2005).
28. Rahmstorf, S. et al. Exceptional twentieth-century slowdown in Atlantic Ocean overturning circulation. *Nat. Clim. Chang.* **5**, 956–956 (2015).
29. Caesar, L., McCarthy, G. D., Thornalley, D. J. R., Cahill, N. & Rahmstorf, S. Current Atlantic Meridional Overturning Circulation weakest in last millennium. *Nat. Geosci.* **14**, 118–120 (2021).
30. Böning, C. W., Behrens, E., Biastoch, A., Getzlaff, K. & Bamber, J. L. Emerging impact of Greenland meltwater on deepwater formation in the North Atlantic Ocean. *Nat. Geosci.* **9**, 523–527 (2016).
31. IPCC. Climate Change 2021 The Physical Science Basis Summary for Policymakers Working Group I Contribution to the Sixth Assessment Report of the Intergovernmental Panel on Climate Change. Climate Change 2021: The Physical Science Basis. (2021).
32. Capotondi, A., Alexander, M. A., Bond, N. A., Curchitser, E. N. & Scott, J. D. Enhanced upper ocean stratification with climate change in the CMIP3 models. *J. Geophys. Res. Ocean.* **117**, 1–23 (2012).
33. Dixon, K. W., Delworth, T. L., Spelman, M. J. & Stouffer, R. J. The influence of transient surface fluxes on North Atlantic overturning in a coupled GCM climate change experiment. *Geophys. Res. Lett.* **26**, 2749–2752 (1999).
34. Haine, T. W. N. et al. Arctic freshwater export: Status, mechanisms, and prospects. *Glob. Planet. Change* **125**, 13–35 (2015).
35. Buckley, M. W. & Marshall, J. Observations, inferences, and mechanisms of the Atlantic Meridional Overturning Circulation: a review. *Rev. Geophys.* **54**, 5–63 (2016).
36. Wang, X., Li, J., Sun, C. & Liu, T. NAO and its relationship with the Northern Hemisphere mean surface temperature in CMIP5 simulations. *J. Geophys. Res.* **122**, 4202–4227 (2017).
37. Trenary, L. & DelSole, T. Does the Atlantic multidecadal oscillation get its predictability from the Atlantic meridional overturning circulation? *J. Clim.* **29**, 5267–5280 (2016).
38. Jungclaus, J., Haak, H., Latif, M. & Mikolajewicz, U. Arctic-North Atlantic Interactions and Multidecadal Variability of the Meridional. *Am. Meteorol. Soc.* **18**, 4013–4031 (2005).
39. Kim, H.-J., An, S.-I. & Kim, D. Timescale-dependent AMOC–AMO relationship in an earth system model of intermediate complexity. *Int. J. Climatol.* **41**, E3298–E3306 (2021).
40. Sévellec, F. & Fedorov, A. V. Optimal excitation of AMOC decadal variability: links to the subpolar ocean. *Prog. Oceanogr.* **132**, 287–304 (2015).
41. Muir, L. C. & Fedorov, A. V. Evidence of the AMOC interdecadal mode related to westward propagation of temperature anomalies in CMIP5 models. *Clim. Dyn.* **48**, 1517–1535 (2017).

42. Frankcombe, L. M., von der Heydt, A. & Dijkstra, H. A. North Atlantic multi-decadal climate variability: an investigation of dominant time scales and processes. *J. Clim.* **23**, 3626–3638 (2010).

43. Griffies, S. M. & Tziperman, E. A linear thermohaline oscillator driven by stochastic atmospheric forcing. *J. Clim.* **8**, 2440–2453 (1995).

44. Timmermann, A., Latif, M., Voss, R. & Grötzner, A. Northern Hemispheric interdecadal variability: a coupled air-sea mode. *J. Clim.* **11**, 1906–1931 (1998).

45. Sun, C., Li, J. & Jin, F. F. A delayed oscillator model for the quasi-periodic multidecadal variability of the NAO. *Clim. Dyn.* **45**, 2083–2099 (2015).

46. Wills, R. C. J., Armour, K. C., Battisti, D. S. & Hartmann, D. L. Ocean-atmosphere dynamical coupling fundamental to the Atlantic Multidecadal Oscillation. *J. Clim.* **32**, 251–272 (2019).

47. O'Reilly, C. H., Zanna, L. & Woollings, T. Assessing external and internal sources of Atlantic multidecadal variability using models, proxy data, and early instrumental indices. *J. Clim.* **32**, 7727–7745 (2019).

48. Eden, C. & Jung, T. North Atlantic interdecadal variability: oceanic response to the North Atlantic oscillation (1865-1997). *J. Clim.* **14**, 676–691 (2001).

49. Latif, M. et al. Is the thermohaline circulation changing? *J. Clim.* **19**, 4631–4637 (2006).

50. Li, J., Sun, C. & Jin, F. F. NAO implicated as a predictor of Northern Hemisphere mean temperature multidecadal variability. *Geophys. Res. Lett.* **40**, 5497–5502 (2013).

51. McCarthy, G. D., Haigh, I. D., Hirschi, J. J. M., Grist, J. P. & Smeed, D. A. Ocean impact on decadal Atlantic climate variability revealed by sea-level observations. *Nature* **521**, 508–510 (2015).

52. Delworth, T. L. & Zeng, F. The impact of the North Atlantic Oscillation on climate through its influence on the Atlantic meridional overturning circulation. *J. Clim.* **29**, 941–962 (2016).

53. Mecking, J. V., Keenlyside, N. S. & Greatbatch, R. J. Stochastically-forced multidecadal variability in the North Atlantic: a model study. *Clim. Dyn.* **43**, 271–288 (2014).

54. Wen, N., Frankignoul, C. & Gastineau, G. Active AMOC–NAO coupling in the IPSL-CM5A-MR climate model. *Clim. Dyn.* **47**, 2105–2119 (2016).

55. Xu, X., Chassignet, E. P. & Wang, F. On the variability of the Atlantic meridional overturning circulation transports in coupled CMIP5 simulations. *Clim. Dyn.* **52**, 6511–6531 (2019).

56. Benedict, J. J., Lee, S. & Feldstein, S. B. Synoptic view of the North Atlantic Oscillation. *J. Atmos. Sci.* **61**, 121–144 (2004).

57. Pinto, J. G. & Raible, C. C. Past and recent changes in the North Atlantic oscillation. *Wiley Interdiscip. Rev. Clim. Chang.* **3**, 79–90 (2012).

58. Olsen, J., Anderson, N. J. & Knudsen, M. F. Variability of the North Atlantic Oscillation over the past 5,200 years. *Nat. Geosci.* **5**, 808–812 (2012).

59. Dickson, R., Lazier, J., Meincke, J., Rhines, P. & Swift, J. Long-term coordinated changes in the convective activity of the North Atlantic. *Prog. Oceanogr.* **38**, 241–295 (1996).

60. Visbeck, M. et al. The ocean's response to North Atlantic oscillation variability. *Geophys. Monogr. Ser.* **134**, 113–145 (2003).

61. Drinkwater, K. F. et al. The Atlantic Multidecadal Oscillation: Its manifestations and impacts with special emphasis on the Atlantic region north of 60°N. *J. Mar. Syst.* **133**, 117–130 (2014).

62. Medhaug, I., Langehaug, H. R., Eldevik, T., Furevik, T. & Bentsen, M. Mechanisms for decadal scale variability in a simulated Atlantic meridional overturning circulation. *Clim. Dyn.* **39**, 77–93 (2012).

63. Grossmann, I. & Klotzbach, P. J. A review of North Atlantic modes of natural variability and their driving mechanisms. *J. Geophys. Res. Atmos.* **114**, 1–14 (2009).

64. Zhang, R. et al. A review of the role of the Atlantic Meridional Overturning Circulation in Atlantic Multidecadal Variability and associated climate impacts. *Rev. Geophys.* **57**, 316–375 (2019).

65. Visbeck, M., Marshall, J. & Jones, H. Dynamics of isolated convective regions in the ocean. *J. Phys. Oceanogr.* **26**, 1721–1734 (1996).

66. Rhein, M., Kieke, D. & Steinfeldt, R. Advection of North Atlantic Deep Water from the Labrador Sea to the southern hemisphere. *J. Geophys. Res. Ocean.* **120**, 2471–2487 (2015).

67. Steffen, E. L. & D'Asaro, E. A. Deep convection in the Labrador Sea as observed by Lagrangian floats. *J. Phys. Oceanogr.* **32**, 475–492 (2002).

68. Killworth, D. P. Deep convection in the world ocean. *Rev. Geophys. Sp. Phys.* **21**, 1–26 (1983).

69. Menary, M. B., Jackson, L. C. & Lozier, M. S. Reconciling the relationship between the AMOC and Labrador Sea in OSNAP observations and climate models. *Geophys. Res. Lett.* **47**, e2020GL089793 (2020).

70. Lozier, M. S. et al. A sea change in our view of overturning in the subpolar North Atlantic. *Science* **363**, 516–521 (2019).

71. Petit, T., Lozier, M. S., Josey, S. A. & Cunningham, S. A. Atlantic deep water formation occurs primarily in the Iceland Basin and Irminger Sea by Local Buoyancy Forcing. *Geophys. Res. Lett.* **47**, 1–9 (2020).

72. Kim, W. M., Yeager, S., Chang, P. & Danabasoglu, G. Low-frequency North Atlantic climate variability in the community earth system model large ensemble. *J. Clim.* **31**, 787–813 (2018).

73. Bracegirdle, T. J., Lu, H., Eade, R. & Woollings, T. Do CMIP5 models reproduce observed low-frequency North Atlantic jet variability? *Geophys. Res. Lett.* **45**, 7204–7212 (2018).

74. Wang, H., Legg, S. A. & Hallberg, R. W. Representations of the Nordic Seas overflows and their large scale climate impact in coupled models. *Ocean Model.* **86**, 76–92 (2015).

75. Koenigk, T. et al. Deep mixed ocean volume in the Labrador Sea in HighResMIP models. *Clim. Dyn.* **57**, 1895–1918 (2021).

76. Ortega, P. et al. Labrador Sea subsurface density as a precursor of multidecadal variability in the North Atlantic: a multi-model study. *Earth Syst. Dyn.* **12**, 419–438 (2021).

77. Roberts, C. D., Garry, F. K. & Jackson, L. C. A multimodel study of sea surface temperature and subsurface density fingerprints of the Atlantic meridional overturning circulation. *J. Clim.* **26**, 9155–9174 (2013).

78. Oldenburg, D., Wills, R. C. J., Armour, K. C., Thompson, L. & Jackson, L. C. Mechanisms of low-frequency variability in north atlantic ocean heat transport and AMOC. *J. Clim.* **34**, 4733–4755 (2021).

79. Caesar, L., Rahmstorf, S., Robinson, A., Feulner, G. & Saba, V. Observed fingerprint of a weakening Atlantic Ocean overturning circulation. *Nature* **556**, 191–196 (2018).

80. Zhang, R. Coherent surface-subsurface fingerprint of the Atlantic meridional overturning circulation. *Geophys. Res. Lett.* **35**, 1–6 (2008).

81. Chen, X. & Tung, K. K. Global surface warming enhanced by weak Atlantic overturning circulation. *Nature* **559**, 387–391 (2018).

82. Sun, C. et al. Atlantic Meridional Overturning Circulation reconstructions and instrumentally observed multidecadal climate variability: a comparison of indicators. *Int. J. Climatol.* **41**, 763–778 (2021).

83. Booth, B. B. B., Dunstone, N. J., Halloran, P. R., Andrews, T. & Bellouin, N. Aerosols implicated as a prime driver of twentieth-century North Atlantic climate variability. *Nature* **484**, 228–232 (2012).

84. Dukhovskoy, D. S. et al. Role of greenland freshwater anomaly in the recent freshening of the Subpolar North Atlantic. *J. Geophys. Res. Ocean.* **124**, 3333–3360 (2019).

85. Hu, S. & Fedorov, A. V. Indian Ocean warming as a driver of the North Atlantic warming hole. *Nat. Commun.* **11**, 1–11 (2020).

86. Lin, P. et al. Two regimes of Atlantic multidecadal oscillation: cross-basin dependent or Atlantic-intrinsic. *Sci. Bull.* **64**, 198–204 (2019).

87. Belkin, I. M., Levitus, S., Antonov, J. & Malmberg, S. A. 'Great Salinity Anomalies' in the North Atlantic. *Prog. Oceanogr.* **41**, 1–68 (1998).

88. Peings, Y., Simpkins, G. & Magnusdottir, G. Multidecadal fluctuations of the North Atlantic Ocean and feedback on the winter climate in CMIP5 control simulations. *J. Geophys. Res. Atmos.* **121**, 2571–2592 (2016).

89. Meehl, G. A. et al. Context for interpreting equilibrium climate sensitivity and transient climate response from the CMIP6 Earth system models. *Sci. Adv.* **6**, 1–11 (2020).

90. Turner, J. S. *Buoyancy Effects in Fluids* (Cambridge University Press, 1973). https://doi.org/10.1017/CBO9780511608827.

91. Gong, H., Wang, L., Chen, W., Chen, X. & Nath, D. Biases of the wintertime Arctic Oscillation in CMIP5 models. *Environ. Res. Lett.* 12, 014001 (2017).

92. Danabasoglu, G. et al. North Atlantic simulations in Coordinated Ocean-ice Reference Experiments phase II (CORE-II). Part I: Mean states. *Ocean Model.* **73**, 76–107 (2014).

93. Gastineau, G. & Frankignoul, C. Cold-season atmospheric response to the natural variability of the Atlantic meridional overturning circulation. *Clim. Dyn.* **39**, 37–57 (2012).

94. Msadek, R. & Frankignoul, C. Atlantic multidecadal oceanic variability and its influence on the atmosphere in a climate model. *Clim. Dyn.* **33**, 45–62 (2009).

95. Behrenfeld, M. J. et al. Climate-driven trends in contemporary ocean productivity. *Nature* **444**, 752–755 (2006).

96. Schmidtko, S., Stramma, L. & Visbeck, M. Decline in global oceanic oxygen content during the past five decades. *Nature* **542**, 335–339 (2017).

97. Kwiatkowski, L. et al. Twenty-first century ocean warming, acidification, deoxygenation, and upper-ocean nutrient and primary production decline from CMIP6 model projections. *Biogeosciences* **17**, 3439–3470 (2020).

98. Ma, X. et al. Evolving AMOC multidecadal variability under different CO2 forcings. *Clim. Dyn.* **57**, 593–610 (2021).

99. Kuzmina, S. I. et al. The North Atlantic Oscillation and greenhouse-gas forcing. *Geophys. Res. Lett.* **32**, 1–4 (2005).

100. Cheng, J. et al. Reduced interdecadal variability of Atlantic Meridional Overturning Circulation under global warming. *Proc. Natl Acad. Sci. USA* **113**, 3175–3178 (2016).

101. Dima, M., Nichita, D. R., Lohmann, G., Ionita, M. & Voiculescu, M. Early-onset of Atlantic Meridional Overturning Circulation weakening in response to atmospheric CO2 concentration. *npj Clim. Atmos. Sci.* **4**, 1–8 (2021).

102. Allan, R. & Ansell, T. A new globally complete monthly historical gridded mean sea level pressure dataset (HadSLP2)_1850–2004. *J. Clim.* **19**, 5816–5842 (2006).

103. Huang, B. et al. Extended reconstructed sea surface temperature version 4 (ERSST.v4). Part I: Upgrades and intercomparisons. *J. Clim.* **28**, 911–930 (2015).

104. Good, S. A., Martin, M. J. & Rayner, N. A. EN4: Quality controlled ocean temperature and salinity profiles and monthly objective analyses with uncertainty estimates. *J. Geophys. Res. Ocean.* **118**, 6704–6716 (2013).

105. Ishii, M., Kimoto, M., Sakamoto, K. & Iwasaki, S.-I. Subsurface temperature and salinity analyses. https://doi.org/10.5065/Y6CR-KW66 (2005).

106. Argo. Argo float data and metadata from Global Data Assembly Centre (Argo GDAC). SEANOE. https://doi.org/10.17882/42182 (2000).

107. Roemmich, D. & Gilson, J. The 2004-2008 mean and annual cycle of temperature, salinity and steric height in the global ocean from the Argo Program. *Prog. Oceanogr.* **82**, 81–100 (2009).

108. Fenty, I. & Wang, O. ECCO ocean mixed layer depth—monthly mean llc90 grid (Version 4 release 4). https://doi.org/10.5067/ECL5M-OML44 (2020).

109. Zhang, R. Latitudinal dependence of Atlantic meridional overturning circulation (AMOC) variations. *Geophys. Res. Lett.* **37**, 1–6 (2010).

110. Ba, J. et al. A multi-model comparison of Atlantic multidecadal variability. *Clim. Dyn.* **43**, 2333–2348 (2014).

111. Zou, S., Lozier, M. S. & Buckley, M. How Is Meridional coherence maintained in the lower limb of the Atlantic Meridional Overturning Circulation? *Geophys. Res. Lett.* **46**, 244–252 (2019).

112. Olson, R., An, S. I., Fan, Y., Evans, J. P. & Caesar, L. North Atlantic observations sharpen meridional overturning projections. *Clim. Dyn.* **50**, 4171–4188 (2018).

113. Bellomo, K., Murphy, L. N., Cane, M. A., Clement, A. C. & Polvani, L. M. Historical forcings as main drivers of the Atlantic multidecadal variability in the CESM large ensemble. *Clim. Dyn.* **50**, 3687–3698 (2018).

114. Murphy, L. N., Bellomo, K., Cane, M. & Clement, A. The role of historical forcings in simulating the observed Atlantic multidecadal oscillation. *Geophys. Res. Lett.* **44**, 2472–2480 (2017).

115. Mann, M. E., Steinman, B. E., Brouillette, D. J. & Miller, S. K. Multidecadal climate oscillations during the past millennium driven by volcanic forcing. *Science* **1019**, 1014–1019 (2021).

116. Otterå, O. H., Bentsen, M., Drange, H. & Suo, L. External forcing as a metronome for Atlantic multidecadal variability. *Nat. Geosci.* **3**, 688–694 (2010).

117. Hurrell, J. W. Decadal trends in the North Atlantic oscillation: regional temperatures and precipitation. *Science* **269**, 676–679 (1995).

118. Pyper, B. J. & Peterman, R. M. Comparison of methods to account for autocorrelation in correlation analyses of fish data. *Can. J. Fish. Aquat. Sci.* **55**, 2127–2140 (1998).

119. Cronin, M. F. & Sprintall, J. Wind And Buoyancy-forced Upper Ocean. *Encycl. Ocean Sci.* 3219–3226 https://doi.org/10.1006/rwos.2001.0157 (2001).

120. Gill, A. E. & Adrian, E. *Atmosphere-ocean Dynamics* Vol. 30 (Academic Press, 1982).

121. Dix, M. et al. CSIRO-ARCCSS ACCESS-CM2 model output prepared for CMIP6 CMIP piControl. V20191112. https://doi.org/10.22033/ESGF/CMIP6.4311 (2019).

122. Ziehn, T. et al. CSIRO ACCESS-ESM1.5 model output prepared for CMIP6 CMIP piControl. V20191214. https://doi.org/10.22033/ESGF/CMIP6.4312 (2019).

123. Lovato, T., Peano, D. & Butenschön, M. CMCC CMCC-ESM2 model output prepared for CMIP6 CMIP piControl. V20210303. https://doi.org/10.22033/ESGF/CMIP6.13241 (2021).

124. Lovato, T. & Peano, D. CMCC CMCC-CM2-SR5 model output prepared for CMIP6 CMIP piControl. V20200609. https://doi.org/10.22033/ESGF/CMIP6.3874 (2020).

125. Voldoire, A. CMIP6 simulations of the CNRM-CERFACS based on CNRM-CM6-1 model for CMIP experiment piControl. V20180321. https://doi.org/10.22033/ESGF/CMIP6.4163 (2018).

126. Voldoire, A. CNRM-CERFACS CNRM-CM6-1-HR model output prepared for CMIP6 CMIP piControl. V20190502. https://doi.org/10.22033/ESGF/CMIP6.4164 (2019).

127. Danabasoglu, G., Lawrence, D., Lindsay, K., Lipscomb, W. & Strand, G. NCAR CESM2 model output prepared for CMIP6 CMIP piControl. V20190726. https://doi.org/10.22033/ESGF/CMIP6.7733 (2019).

128. Danabasoglu, G. NCAR CESM2-FV2 model output prepared for CMIP6 CMIP piControl. V20190814. https://doi.org/10.22033/ESGF/CMIP6.11301 (2019).

129. Danabasoglu, G. NCAR CESM2-WACCM model output prepared for CMIP6 CMIP piControl. V20190726. https://doi.org/10.22033/ESGF/CMIP6.10094 (2019).

130. Danabasoglu, G. NCAR CESM2-WACCM-FV2 model output prepared for CMIP6 CMIP piControl. V20191010. https://doi.org/10.22033/ESGF/CMIP6.11302 (2019).

131. Bader, D. C., Leung, R., Taylor, M. & McCoy, R. B. E3SM-Project E3SM1.0 model output prepared for CMIP6 CMIP piControl. V20191002. https://doi.org/10.22033/ESGF/CMIP6.4499 (2018).

132. Bader, D. C., Leung, R., Taylor, M. & McCoy, R. B. E3SM-Project E3SM1.1 model output prepared for CMIP6 CMIP piControl. V20191028. https://doi.org/10.22033/ESGF/CMIP6.11489 (2019).

133. Li, L. CAS FGOALS-g3 model output prepared for CMIP6 CMIP piControl. V20191125. https://doi.org/10.22033/ESGF/CMIP6.3448 (2019).

134. NASA Goddard Institute for Space Studies (NASA/GISS). NASA-GISS GISS-E2.1G model output prepared for CMIP6 CMIP piControl. V20190820. https://doi.org/10.22033/ESGF/CMIP6.7380 (2018).

135. NASA Goddard Institute for Space Studies (NASA/GISS). NASA-GISS GISS-E2-2-G model output prepared for CMIP6 CMIP piControl. V20191115. https://doi.org/10.22033/ESGF/CMIP6.7382 (2019).

136. Ridley, J., Menary, M., Kuhlbrodt, T., Andrews, M. & Andrews, T. MOHC HadGEM3-GC31-LL model output prepared for CMIP6 CMIP piControl. V20190814. https://doi.org/10.22033/ESGF/CMIP6.6294 (2018).

137. Ridley, J., Menary, M., Kuhlbrodt, T., Andrews, M. & Andrews, T. MOHC HadGEM3-GC31-MM model output prepared for CMIP6 CMIP piControl. V20191004. https://doi.org/10.22033/ESGF/CMIP6.6297 (2019).

138. Boucher, O. et al. IPSL IPSL-CM6A-LR model output prepared for CMIP6 CMIP piControl. V20190628. https://doi.org/10.22033/ESGF/CMIP6.5251 (2018).

139. Tatebe, H. & Watanabe, M. MIROC MIROC6 model output prepared for CMIP6 CMIP piControl. V20200420. https://doi.org/10.22033/ESGF/CMIP6.5711 (2018).

140. Hajima, T. et al. MIROC MIROC-ES2L model output prepared for CMIP6 CMIP piControl. V20210126. https://doi.org/10.22033/ESGF/CMIP6.5710 (2019).

141. Neubauer, D. et al. HAMMOZ-Consortium MPI-ESM1.2-HAM model output prepared for CMIP6 CMIP piControl. V20191208. https://doi.org/10.22033/ESGF/CMIP6.5037 (2019).

142. Jungclaus, J. et al. MPI-M MPI-ESM1.2-HR model output prepared for CMIP6 CMIP piControl. V20190821. https://doi.org/10.22033/ESGF/CMIP6.6674 (2019).

143. Wieners, K.-H. et al. MPI-M MPI-ESM1.2-LR model output prepared for CMIP6 CMIP piControl. V20191207. https://doi.org/10.22033/ESGF/CMIP6.6675 (2019).

144. Yukimoto, S. et al. MRI MRI-ESM2.0 model output prepared for CMIP6 CMIP piControl. V20191211. https://doi.org/10.22033/ESGF/CMIP6.6900 (2019).

145. Bethke, I. et al. NCC NorCPM1 model output prepared for CMIP6 CMIP piControl. V20190914. https://doi.org/10.22033/ESGF/CMIP6.10896 (2019).

146. Seland, Ø. et al. NCC NorESM2-LM model output prepared for CMIP6 CMIP piControl. V20191108. https://doi.org/10.22033/ESGF/CMIP6.8217 (2019).

147. Bentsen, M. et al. NCC NorESM2-MM model output prepared for CMIP6 CMIP piControl. V20200102. https://doi.org/10.22033/ESGF/CMIP6.8221 (2019).

148. Tang, Y. et al. MOHC UKESM1.0-LL model output prepared for CMIP6 CMIP piControl. V20190821. https://doi.org/10.22033/ESGF/CMIP6.6298 (2019).

149. Mulcahy, J. et al. MOHC UKESM1.1-LL model output prepared for CMIP6 CMIP piControl. V20220509. https://doi.org/10.22033/ESGF/CMIP6.16823 (2022).

150. Swart, N. C. et al. CCCma CanESM5 model output prepared for CMIP6 CMIP piControl. V20190605. https://doi.org/10.22033/ESGF/CMIP6.3673 (2019).

151. Swart, N. C. et al. CCCma CanESM5-CanOE model output prepared for CMIP6 CMIP piControl. V20191211. https://doi.org/10.22033/ESGF/CMIP6.10266 (2019).

152. EC-Earth-Consortium (EC-Earth). EC-Earth3-LR model output prepared for CMIP6 CMIP piControl. V20191218. https://doi.org/10.22033/ESGF/CMIP6.4847 (2019).

153. Lorenz, S. et al. MPI-M ICON-ESM-LR model output prepared for CMIP6 CMIP piControl. V20210724. https://doi.org/10.22033/ESGF/CMIP6.6673 (2021).

154. Volodin, E. et al. INM INM-CM4-8 model output prepared for CMIP6 CMIP piControl. V20190605. https://doi.org/10.22033/ESGF/CMIP6.5080 (2019).

155. Volodin, E. et al. INM INM-CM5-0 model output prepared for CMIP6 CMIP piControl. V20190628. https://doi.org/10.22033/ESGF/CMIP6.5081 (2019).

156. Seferian, R. CNRM-CERFACS CNRM-ESM2-1 model output prepared for CMIP6 CMIP piControl. V20180423. https://doi.org/10.22033/ESGF/CMIP6.4165 (2018).

157. Bader, D. C., Leung, R., Taylor, M. & McCoy, R. B. E3SM-Project E3SM1.1ECA model output prepared for CMIP6 CMIP piControl. V20200128. https://doi.org/10.22033/ESGF/CMIP6.11490 (2019).

158. EC-Earth-Consortium (EC-Earth). EC-Earth3 model output prepared for CMIP6 CMIP piControl. V20190712. https://doi.org/10.22033/ESGF/CMIP6.4842 (2019).

159. EC-Earth-Consortium (EC-Earth). EC-Earth3-AerChem model output prepared for CMIP6 CMIP piControl. V20201228. https://doi.org/10.22033/ESGF/CMIP6.4843 (2020).

160. EC-Earth-Consortium (EC-Earth). EC-Earth-3-CC model output prepared for CMIP6 CMIP piControl. V20200723. https://doi.org/10.22033/ESGF/CMIP6.4844 (2021).

161. EC-Earth-Consortium (EC-Earth). EC-Earth3-Veg model output prepared for CMIP6 CMIP piControl. V20190619. https://doi.org/10.22033/ESGF/CMIP6.4848.

162. EC-Earth-Consortium (EC-Earth). EC-Earth3-Veg-LR model output prepared for CMIP6 CMIP piControl. V20200213. https://doi.org/10.22033/ESGF/CMIP6.4849.

AUTHOR CONTRIBUTIONS

H.-J.K. performed the analyses and wrote the original manuscript. H.-J.K., S.-I.A., M.-K.S., and J.-H.P. conceived the idea. D.K., Y.C., and J.-S.K. reviewed and helped revise the manuscript. All authors participated in the interpretation of the results and editing of the manuscript.

COMPETING INTERESTS

The authors declare no competing interests.

ADDITIONAL INFORMATION

Supplementary information The online version contains supplementary material available at https://doi.org/10.1038/s41612-023-00354-x.

Correspondence and requests for materials should be addressed to Soon-Il An.

Reprints and permission information is available at http://www.nature.com/reprints

Publisher's note Springer Nature remains neutral with regard to jurisdictional claims in published maps and institutional affiliations.